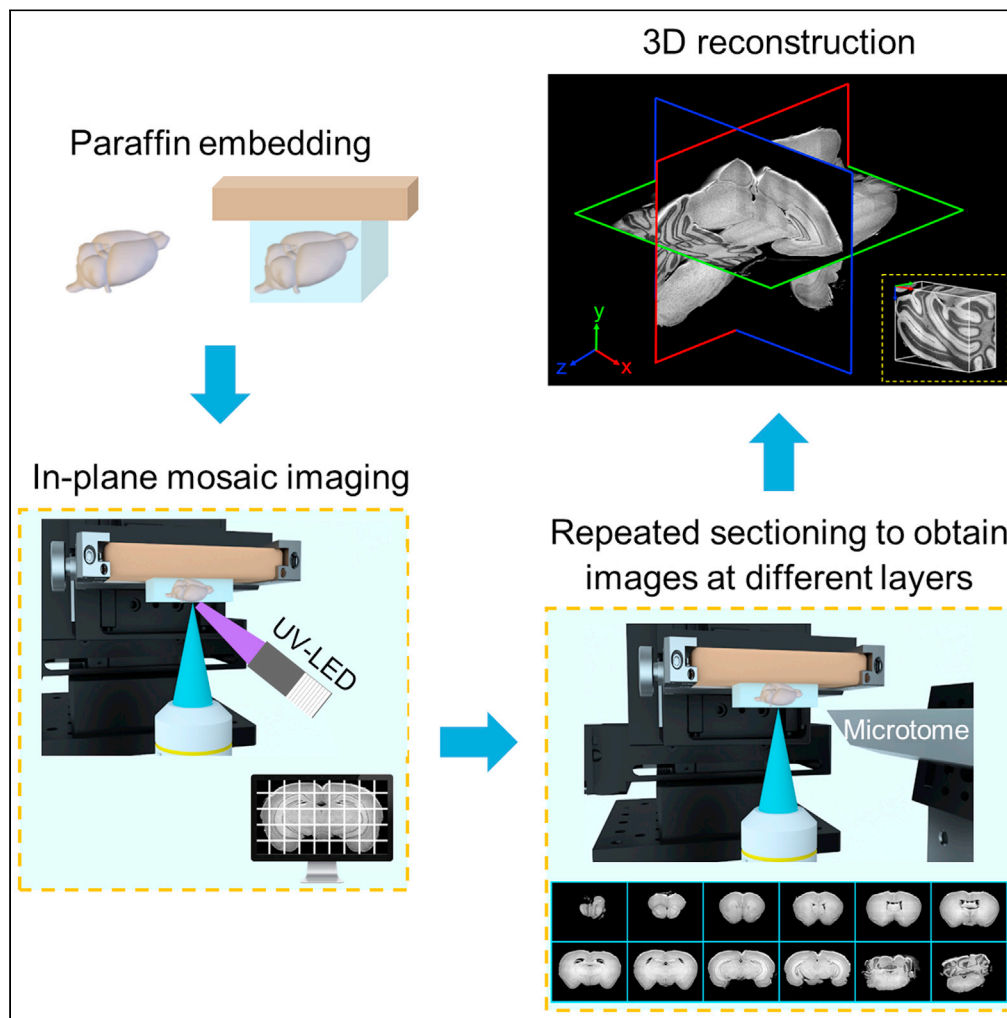


Article

Three-dimensional label-free histological imaging of whole organs by microtomy-assisted autofluorescence tomography



Yan Zhang, Lei Kang, Wentao Yu, Victor T.C. Tsang, Terence T.W. Wong

ttwong@ust.hk

Highlights
MATE enables label-free 3D imaging of whole organs without tissue staining or clearing

Various anatomical structures can be simultaneously visualized in a label-free manner

MATE reveals diagnostic features comparable with the gold standard histology

MATE facilitates comprehensive histopathological analysis at the subcellular level

Zhang et al., iScience 25, 103721
January 21, 2022 © 2021 The Author(s).
<https://doi.org/10.1016/j.isci.2021.103721>

Article

Three-dimensional label-free histological imaging of whole organs by microtomy-assisted autofluorescence tomography

Yan Zhang,¹ Lei Kang,¹ Wentao Yu,¹ Victor T.C. Tsang,¹ and Terence T.W. Wong^{1,2,*}

SUMMARY

Three-dimensional (3D) histology is vitally important to characterize disease-induced tissue heterogeneity at the individual cell level. However, it remains challenging for both high-throughput 3D imaging and volumetric reconstruction. Here we propose a label-free, cost-effective, and ready-to-use 3D histological imaging technique, termed microtomy-assisted autofluorescence tomography with ultraviolet excitation (MATE). With the combination of block-face imaging and serial microtome sectioning, MATE can achieve rapid and label-free imaging of paraffin-embedded whole organs at an acquisition speed of 1 cm³ per 4 h with a voxel resolution of 1.2 × 1.2 × 10 μm³. We demonstrate that MATE enables simultaneous visualization of cell nuclei, fiber tracts, and blood vessels in mouse/human brains without tissue staining or clearing. Moreover, diagnostic features, including nuclear size and packing density, can be quantitatively extracted with high accuracy. MATE is augmented to the current slide-based 2D histology, holding great promise to facilitate histopathological interpretation at the organelle level.

INTRODUCTION

Conventional slide-based two-dimensional (2D) histology is commonly used clinically. However, it fails to provide sufficient representation of large and bulky tissues. On the contrary, 3D histology is vital to study structural changes volumetrically at the cellular level, allowing accurate diagnosis of continuously spreading tumor strands (Moehrle et al., 2006). Yet, conventional 3D histology (Roberts et al., 2012; Wang et al., 2015) based on image registration of serial histochemically stained thin tissue slices is fundamentally slow, labor intensive, and inaccurate owing to the inevitable tissue ruptures during slide preparation, which further poses a challenge for the registration of adjacent slices during volumetric reconstruction (Pichat et al., 2018).

Modern advancements in optical microscopy, data processing, and 3D visualization pave a way for multi-scale 3D analysis of complex tissue networks at microscopic resolution. However, owing to light scattering and absorption, traditional optical imaging techniques (Conchello and Lichtman, 2005; Helmchen and Denk, 2005; Mertz, 2011) can only image tens to hundreds of microns deep into the tissue, hindering their applications of 3D imaging of whole organs. To increase the accessible imaging depth, light-sheet fluorescence microscopy of chemically cleared tissues (Huisken et al., 2004; Dodt et al., 2007; Renier et al., 2014; Tomer et al., 2014) has been extensively utilized for rapid volumetric imaging. However, the imaging quality is significantly degraded with depth owing to inhomogeneous tissue clearing (Narasimhan et al., 2015). In addition, slow diffusion and limited penetration of fluorescent probes into the cleared tissues is a common issue (Marx, 2016). Alternatively, imaging systems based on the integration of serial mechanical sectioning provide a new strategy to overcome the depth limitation. Serial two-photon tomography (STPT) (Ragan et al., 2012; Economo et al., 2016), block-face serial microscopy tomography (FAST) (Seiriki et al., 2017), wide-field large-volume tomography (WVT) (Gong et al., 2016), micro-optical sectioning tomography (MOST) (Li et al., 2010), and fluorescence MOST (fMOST) (Gong et al., 2013) are all examples of this approach. With the combination of ultra-thin sectioning and line-scan imaging on a knife-edge, MOST and fMOST enable one to image resin-embed whole mouse brains at 0.33 × 0.33 × 1 μm³ voxel resolution within ~10 days (Li et al., 2010). In contrast, block-face imaging systems (i.e., STPT, FAST, and WVT), similar to serial block-face scanning electron microscopy (Denk and Horstmann, 2004), are implemented by

¹Translational and Advanced Bioimaging Laboratory, Department of Chemical and Biological Engineering, The Hong Kong University of Science and Technology, Kowloon, Hong Kong, China

²Lead contact

*Correspondence: ttwong@ust.hk

<https://doi.org/10.1016/j.isci.2021.103721>



alternating cycles of en face imaging of a tissue block and mechanical removal of the imaged surface. These systems considerably accelerate the 3D imaging pipeline by adopting a relatively large slicing interval, and the captured serial block-face images are inherently registered, ensuring an accurate volumetric reconstruction. For instance, by using spinning disk confocal microscopy, FAST demonstrates an unprecedented speed that can achieve whole-brain imaging at $0.7 \times 0.7 \times 5 \mu\text{m}^3$ voxel resolution within 2.4 h (Seiriki et al., 2017). The aforementioned systems are powerful tools to study 3D microanatomical structures of large tissues. However, they all require well-regulated and time-consuming protocols regarding tissue preparation, such as clearing (Richardson and Lichtman, 2015), staining, and embedding (Zheng et al., 2019) of an intact organ, making it challenging to be integrated into the current histology workflow.

Therefore, label-free 3D imaging with minimum tissue preparation is highly desired in modern clinical settings. Figure S1 shows detailed comparisons between different label-free 3D imaging techniques. Macroscopic imaging methods, including X-ray computed tomography (Salvolini et al., 2000), magnetic resonance imaging (MRI) (Xiao et al., 2011), and photoacoustic tomography (Li et al., 2016) can achieve non-destructive tomographic imaging of whole organs within several to tens of minutes. However, they are not suitable for probing molecular targets as desired in standard histopathology due to the low spatial resolution, which is typically on the order of tens of micrometers. In contrast, microscopic imaging methods are capable of providing rich cellular contents that are crucial for diagnosis. For instance, microscale MRI (Davis et al., 2018) and X-ray microcomputed tomography (μCT) (Katsamenis et al., 2019) are powerful tools that enable non-destructive 3D anatomical imaging of centimeter-scale tissues within several hours with a resolution reaching $\sim 1 \mu\text{m}$. However, they require expensive hardware such as strong and gradient magnetic field sources or X-ray tubes, which are not readily available in most settings. In addition, the contrast in MRI images is strongly perturbed by microscale magnetic field gradients in cells and tissues; thus, it has not been extensively investigated for subcellular histological imaging. Furthermore, it is challenging to achieve high-quality imaging of soft tissues with μCT owing to the low X-ray attenuation (Juliana et al., 2015; Busse et al., 2018). Serial optical coherence microscopy (Min et al., 2020), which combines optical interferometry and serial sectioning, enables label-free whole-brain imaging at $1 \times 1 \times 4 \mu\text{m}^3$ voxel resolution within 3 h. However, the reflectance-based nuclear contrast is relatively low. Besides, microtomy-assisted photoacoustic microscopy (Wong et al., 2017) enables whole-brain imaging at $0.91 \times 0.91 \times 20 \mu\text{m}^3$ voxel resolution with an excellent nuclear contrast provided by ultraviolet (UV) excitation. However, the long acquisition time (>15 days) eventually hinders its utility as a routine tissue analysis approach.

To this end, we propose a label-free, automated, and ready-to-use 3D histological imaging method, termed microtomy-assisted autofluorescence tomography with UV excitation (MATE). Rich endogenous fluorophores (Monici, 2005), including reduced nicotinamide adenine dinucleotide, flavin coenzymes, structural proteins, aromatic amino acids, porphyrins, and lipopigments, naturally fluoresce with deep-UV excitation (Jamme et al., 2013), generating an intrinsic absorption-based contrast for label-free histological imaging. In addition, moderate optical sectioning strength ($\sim 10 \mu\text{m}$ [Meinhardt et al., 2008]) provided by UV surface excitation (Fereidouni et al., 2017; Yoshitake et al., 2018; Guo et al., 2019) allows MATE to be integrated with block-face imaging and microtome sectioning to enhance the accessible imaging depth. The automated MATE system provides serial registration-free block-face images of formalin-fixed and paraffin-embedded (FFPE) whole organs without tissue staining or clearing, achieving rapid 3D imaging of a whole mouse brain at $1.2 \times 1.2 \times 10 \mu\text{m}^3$ voxel resolution within 3.5 h, generating a brain atlas like dataset that consists of 900 serial coronal sections with an overall data size of ~ 300 gigabytes. Here, we demonstrate that MATE enables simultaneous visualization of various anatomical structures, including cell nuclei, fiber tracts, and blood vessels in mouse/human brains with high fidelity. Moreover, diagnostic features, such as nuclear size and packing density, can be quantitatively extracted from MATE images with high accuracy. The high speed, low cost, and ease-of-use features of MATE demonstrate its great potential as a routine tissue analysis tool that can potentially fit into the current histology workflow, facilitating the applications of histopathological interpretation at the cellular level to analyze complex tissue networks.

RESULTS

MATE system for whole-organ imaging and sectioning

MATE is configured in a reflection mode to accommodate tissues with any size and thickness (Figure 1). A UV light-emitting diode (LED) with 285 nm wavelength is implemented for the excitation of endogenous fluorophores based on intrinsic absorption. The wavelength 285 nm is near the absorption maximum of DNA/RNA molecules (Yao and Wang, 2013); thus, using a 285-nm source would enable a high label-free nuclear contrast in MATE images (Figure S2). With oblique illumination, we circumvent the use of UV-transmitting

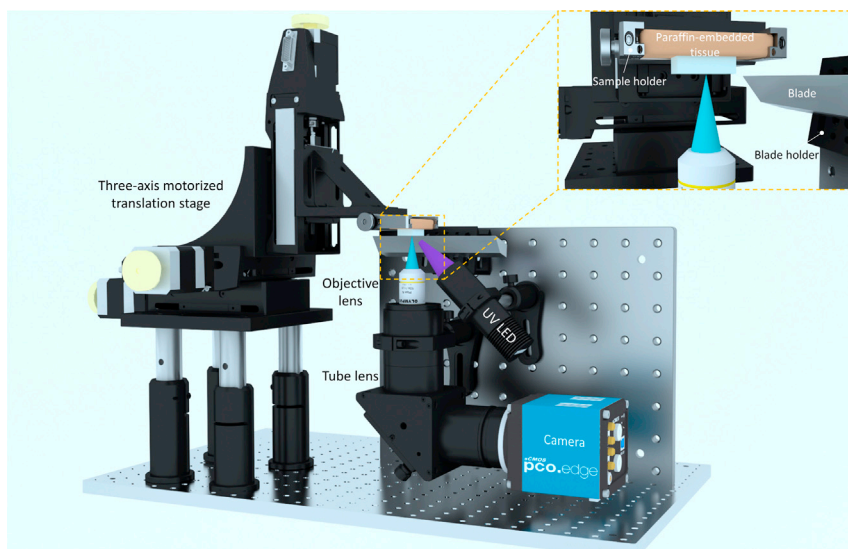


Figure 1. Schematic of the MATE system for whole-organ imaging and sectioning

The UV light from a UV-LED is focused onto the bottom surface of a block specimen, which is clamped toward the objective lens by an adjustable sample holder and rigidly mounted on a three-axis motorized translation stage to control both the scanning for in-plane imaging and tissue sectioning. The excited intrinsic fluorescence signals from the exposed tissue surface are collected by an objective lens, refocused by a tube lens, and subsequently detected by a monochromatic camera. The imaged surface is then sectioned by a laboratory-built microtome (blade) so that a new surface is exposed for imaging. This process is repeated until the entire tissue block is imaged.

optics and fluorescence filters because the backscattered UV light is naturally blocked by the glass objective and tube lens, which are spectrally opaque at 285 nm. The FFPE block specimen is clamped toward the objective lens by an adjustable sample holder and rigidly mounted on a three-axis motorized stage to control both the scanning for in-plane mosaic imaging and tissue sectioning by a laboratory-built microtome (inset of Figure 1). The alternating cycles of en face imaging of a tissue block and mechanical removal of the imaged surface are repeated until the whole block specimen is captured. With the synchronization of block-face imaging and microtome sectioning, the automated MATE imaging system provides serial distortion- and registration-free z stack images evenly spaced at a 10- μm interval, enabling rapid and label-free 3D imaging at an acquisition speed of 1 cm^3 per 4 h with a measured lateral resolution of 1.2 μm (Figure S3).

MATE imaging of an intact FFPE mouse brain block

The performance of MATE is initially validated by imaging FFPE thin slices of mouse kidney/liver tissues (Figure S4). The microtome-sectioned thin tissue slices are deparaffinized to minimize paraffin-induced fluorescence for MATE imaging. A variety of anatomical structures, including renal tubules, Bowman's space, and glomerulus in mouse kidney (Figures S4B–S4D), and hepatocytes, hepatic sinusoids, and erythrocytes in mouse liver (Figures 4I–4K), are clearly identified. After MATE imaging, the slices are histochemically stained by hematoxylin and eosin (H&E) and imaged with a bright-field microscope to obtain the corresponding histological images for comparison (Figures S4E–S4g and S4L–S4N). Multiple similarities are revealed in MATE and H&E-stained images; despite that, the nucleolar structures in mouse liver are less visible in MATE images. Pearson correlation coefficient of 0.9 is calculated from Figures S4B and S4E, validating the feasibility of using tissue's autofluorescence as an intrinsic contrast for label-free histological imaging.

The moderate optical sectioning strength provided by UV surface excitation enables MATE to be utilized for slide-free histological imaging, which is validated by imaging an FFPE mouse brain block (Figures S5 and Video S1). The mouse brain block is imaged by the MATE system (Figures S5A–S5F) and subsequently sectioned at the surface by a microtome with 7- μm thickness to obtain the corresponding H&E-stained images for comparison (Figures S5G–S5I). Although the slide-based histological images cannot exactly replicate the imaged surface by MATE owing to the different imaging depth and tissue distortion, the histological features, including isocortex, hippocampus, thalamus, and cortical amygdala are still remarkably similar. Nuclear features, such as cross-sectional area and intercellular distance, are extracted from MATE and H&E-stained images (e.g., Figures S5B and S5H).

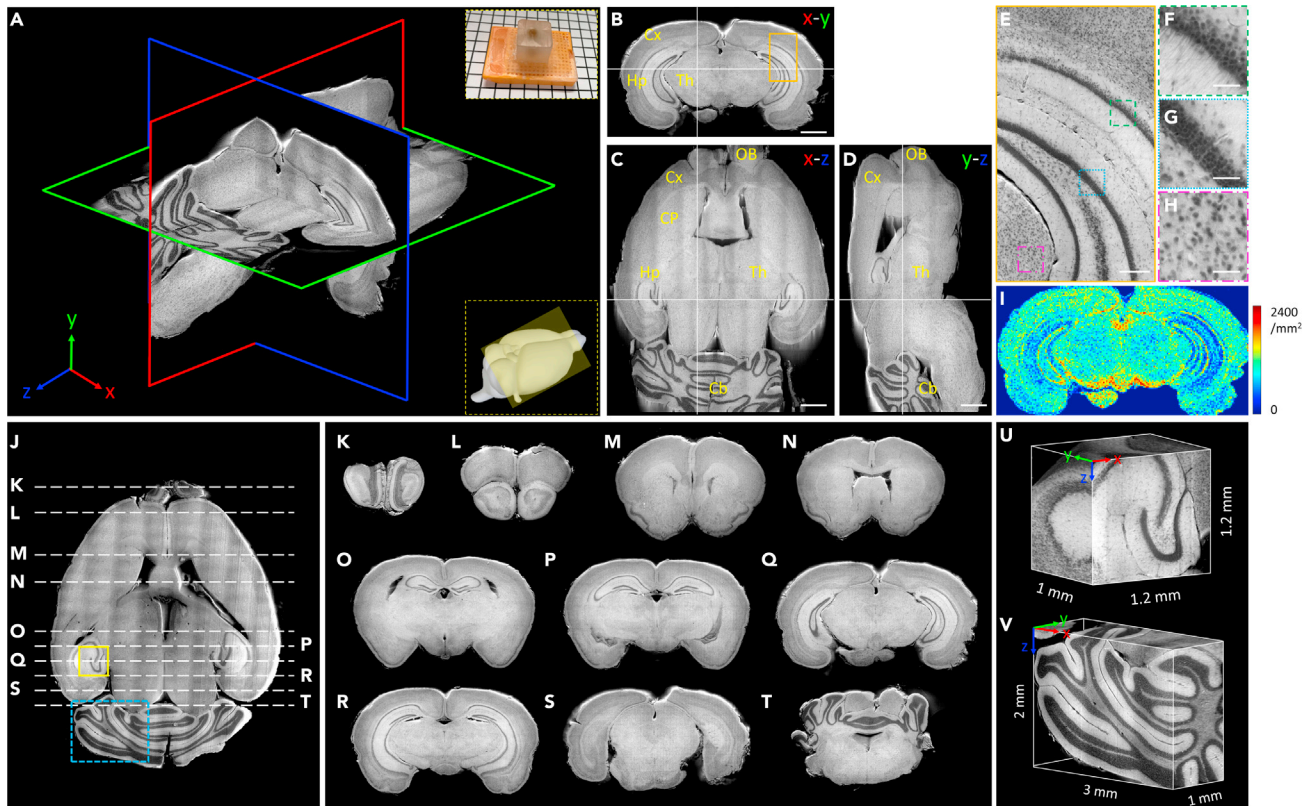


Figure 2. 3D label-free MATE imaging of an intact mouse brain embedded in an FFPE block

(A) A 3D model with orthogonal views of the imaged whole mouse brain. The top inset shows the photograph of the specimen, and the bottom inset indicates the imaging area of a 3D mouse brain model (yellow shaded region).
 (B–D) The corresponding coronal view (x-y plane), transverse view (x-z plane), and sagittal view (y-z plane) of the imaged brain, respectively. Crosshairs are linked in three orthogonal views, and anatomical structures are annotated in each view. OB, olfactory bulb; Cx, cerebral cortex; CP, caudate putamen; Hp, hippocampus; Th, thalamus; Cb, cerebellum. Scale bars: 1 mm.
 (E) A zoomed-in MATE image of the orange solid region in (B). Scale bar: 200 μm .
 (F–H) Zoomed-in MATE images of green, blue, and magenta dashed regions in (E), respectively. Scale bar: 50 μm .
 (I) A nuclear density map calculated from (B).
 (J) A transverse view of the brain volume.
 (K–T) Ten representative coronal sections with the relative positions marked in J.
 (U and V) Volumetric rendering of yellow solid and blue dashed regions in (J), respectively.

for quantitative analysis. The difference between these two distributions of nuclear features is evaluated by Wilcoxon rank-sum test under a significance level of 0.05. Our results suggest that the nuclear features extracted from MATE agree fairly well with the H&E-stained histological image (Figure S5M and S5N), validating the accuracy of the information that can be provided by MATE.

To determine the optimal sectioning interval for 3D whole-brain imaging, the imaging depth of MATE is estimated by leveraging the fact that nuclear count is linearly proportional to the accessible tissue imaging depth. First, an FFPE mouse brain block is imaged by MATE (Figure S6A). Then, the same tissue block is consecutively sectioned at the block surface with 7 μm thickness and subsequently stained with H&E to obtain three adjacent slices (Figures S6B–S6D), which reveal the nuclear distribution within a depth range of 21 μm in total. The ratio of the nuclear count in the H&E-stained images within a given depth range to that in the MATE image is calculated to be closest to unity for a depth range of 7 μm (Figure S6I), suggesting that the imaging depth of MATE is within 10 μm .

The full capacity of MATE for 3D high-resolution imaging is demonstrated in Figure 2. An intact FFPE mouse brain block (top inset of Figure 2A) is imaged by MATE at 10- μm sectioning interval within 3.5 h, generating a brain atlas-like dataset consisting of \sim 900 serial registration-free coronal sections with an

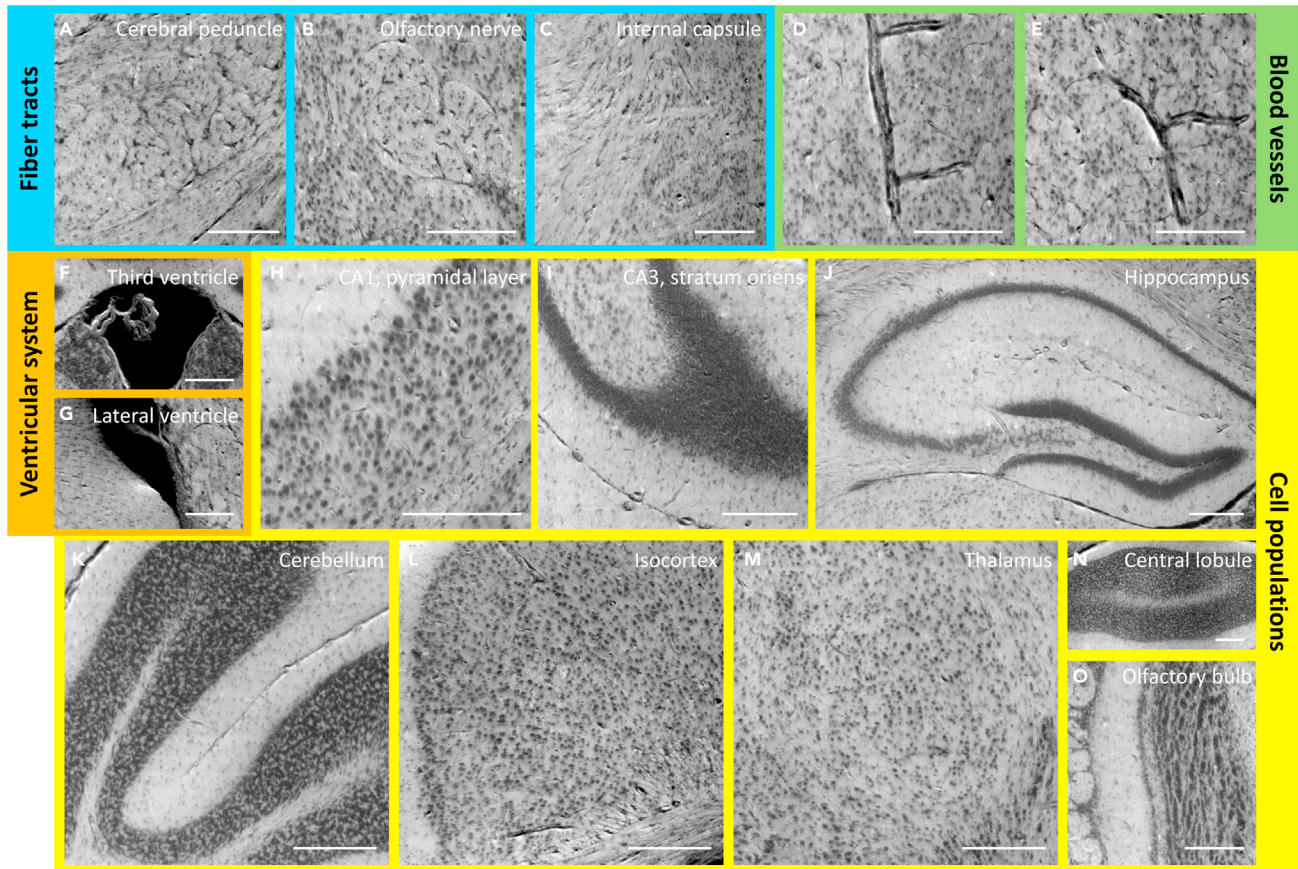


Figure 3. Image gallery of features extracted from label-free MATE images of the FFPE mouse brain block

(A–C) Fiber tracts. Scale bars: 200 μm .

(D and E) Blood vessels. Scale bars: 200 μm .

(F and G) Ventricular system. Scale bars: 200 μm .

(H–O) Cell populations located at different regions across the whole brain. Scale bars: 200 μm .

overall size of ~ 300 gigabytes (Video S2). The 3D model with orthogonal views of the imaged whole brain is shown in Figure 2A. Anatomical structures including cerebellum, cerebral cortex, hippocampus, thalamus, and olfactory bulb are clearly visualized in the coronal (Figure 2B), transverse (Figure 2C) and sagittal (Figure 2D) images. The densely packed cell nuclei in the hippocampus (Figures 2E–2G) can be resolved individually with a lateral resolution of 1.2 μm . Each nucleus in the coronal section can be localized by Jerman's spherical enhancement filter (Jerman et al., 2015), which is based on the ratio of multiscale Hessian eigenvalues, generating a nuclear density map across the whole coronal section (Figures 2I and S7). Note that the nuclear count is not absolutely accurate because the vascular cross sections, which present similar brightness to cell nuclei in the MATE images, are also extracted by Jerman's filter. We believe that integrating with advanced segmentation neural networks would enable a more faithful statistical analysis. Ten representative coronal sections with the relative positions marked in a transverse view (Figure 2J) are shown in Figures 2K–2T. Volumetric rendering of the hippocampus and cerebellum indicated by yellow solid and blue dashed regions in Figure 2J are demonstrated in Figures 2U and 2V, respectively.

Figure 3 shows a variety of histological features extracted collectively from the imaged mouse brain block, showing in the coronal view. Fiber tracts (Figures 3A–3C), blood vessels (Figures 3D and 3E), ventricular system (Figures 3F and 3G), and cell populations (Figures 3H–3O) located at different regions across the whole brain are simultaneously visualized in MATE images with high fidelity in a label-free manner. This unique capability of MATE enables comprehensive 3D histopathological analysis of complex whole organs, thus holding great promise for the investigation of structural connectivity and heterogeneity involved in many disease processes. To further explore the effect of different embedding materials, a formalin-fixed

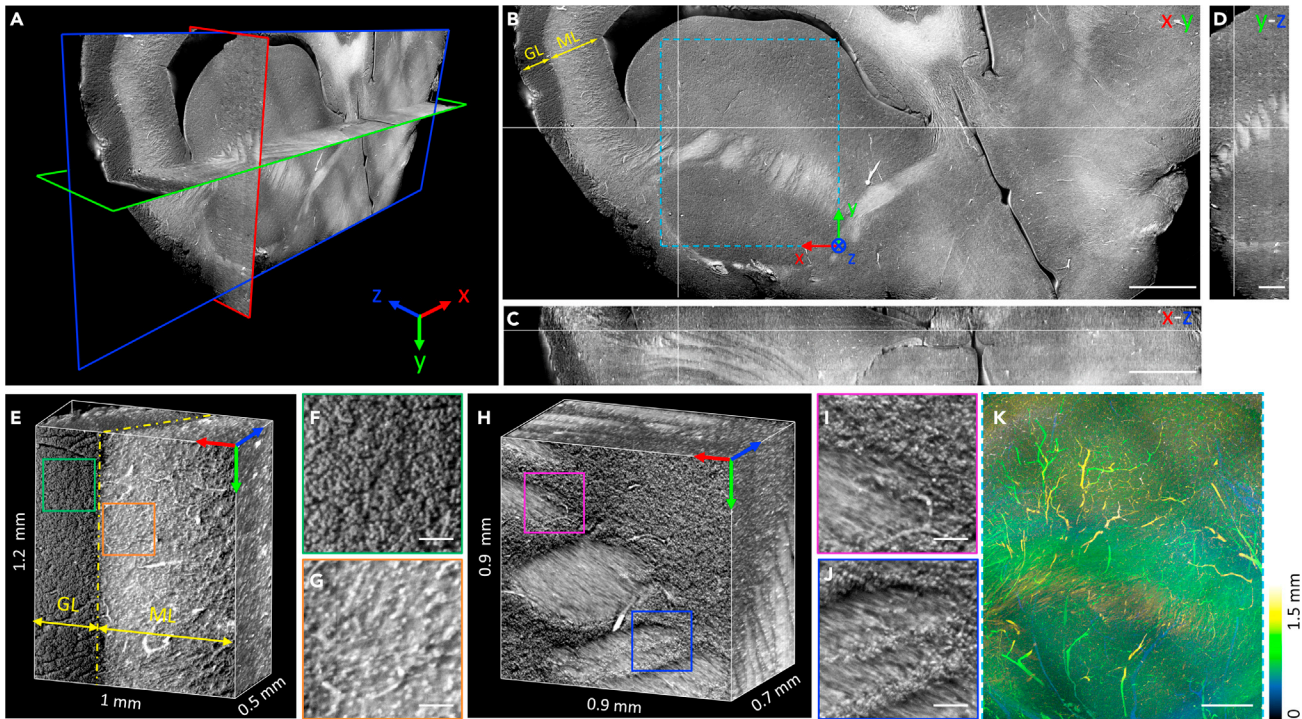


Figure 4. 3D label-free MATE imaging of an FFPE human brain block

(A–D) A 3D model generated by MATE imaging with its corresponding orthogonal views of an imaged human brain block. Crosshairs are linked in three orthogonal views. Scale bars: 1 mm (B,C), 500 μ m (D).

(E) Volumetric rendering of a portion of the cerebellar cortex, with the boundary between granular layer (GL) and molecular layer (ML) marked by a yellow dashed line.

(F and G) Zoomed-in MATE images of green and orange solid regions in (E), respectively. Scale bars: 50 μ m.

(H) Volumetric rendering of fiber pathways in the white matter.

(I and J) Zoomed-in MATE images of magenta and blue solid regions in H, respectively. Scale bars: 50 μ m.

(K) Vascular network with color-coded depth obtained by 3D projection of the blue dashed region in B. Scale bar: 500 μ m.

and agarose-embedded mouse brain is sectioned by a vibratome with 200 μ m thickness for MATE imaging. Two representative coronal sections are shown in [Figures S8A–S8E](#), and the corresponding features extracted from a paraffin-embedded mouse brain are utilized for comparison ([Figures S8F–S8H](#)). An obvious distinction is observed that autofluorescence from fiber tracts (e.g., internal capsule and cerebral peduncle) and myelin-rich globus pallidus is significantly quenched by the tissue-infiltrative paraffin, resulting in a homogeneous intensity distribution across the whole brain. In addition, tissue shrinkage is inevitable during paraffin embedding, with a reported percentage of shrinkage ranging from 10% to 27% ([Boonstra et al., 1983](#); [Tran et al., 2015](#)). Although agarose-embedded tissues may be more suitable for MATE imaging, the sectioning quality is far inferior to that with paraffin-embedded tissues at a 10- μ m slicing interval. We believe that integrating a vibrating blade (i.e., vibratome) with agarose-embedded tissues can further improve the slicing and imaging quality.

MATE imaging of an FFPE human brain block

High-resolution 3D MATE imaging of an FFPE human brain block is shown in [Figure 4](#). The block specimen with a dimension of $11 \times 4.5 \times 1.5 \text{ mm}^3$ is imaged by MATE at a 10- μ m sectioning interval within 30 min, generating a dataset consisting of 150 serial sections with an overall size of ~ 35 gigabytes ([Video S3](#)). The 3D model of the imaged volume is illustrated in [Figure 4A](#), with its corresponding orthogonal views shown in [Figures 4B–4D](#). Volumetric rendering of a portion of the cerebellar cortex ([Figure 4E](#)) outlines a clear boundary between the granular layer and molecular layer. With cellular resolution, the densely packed granule cells ([Figure 4F](#)) are resolved individually. Structural connectivity in the white matter is clearly revealed in [Figure 4H](#), where fiber pathways with the intertwined cell populations are visualized with high

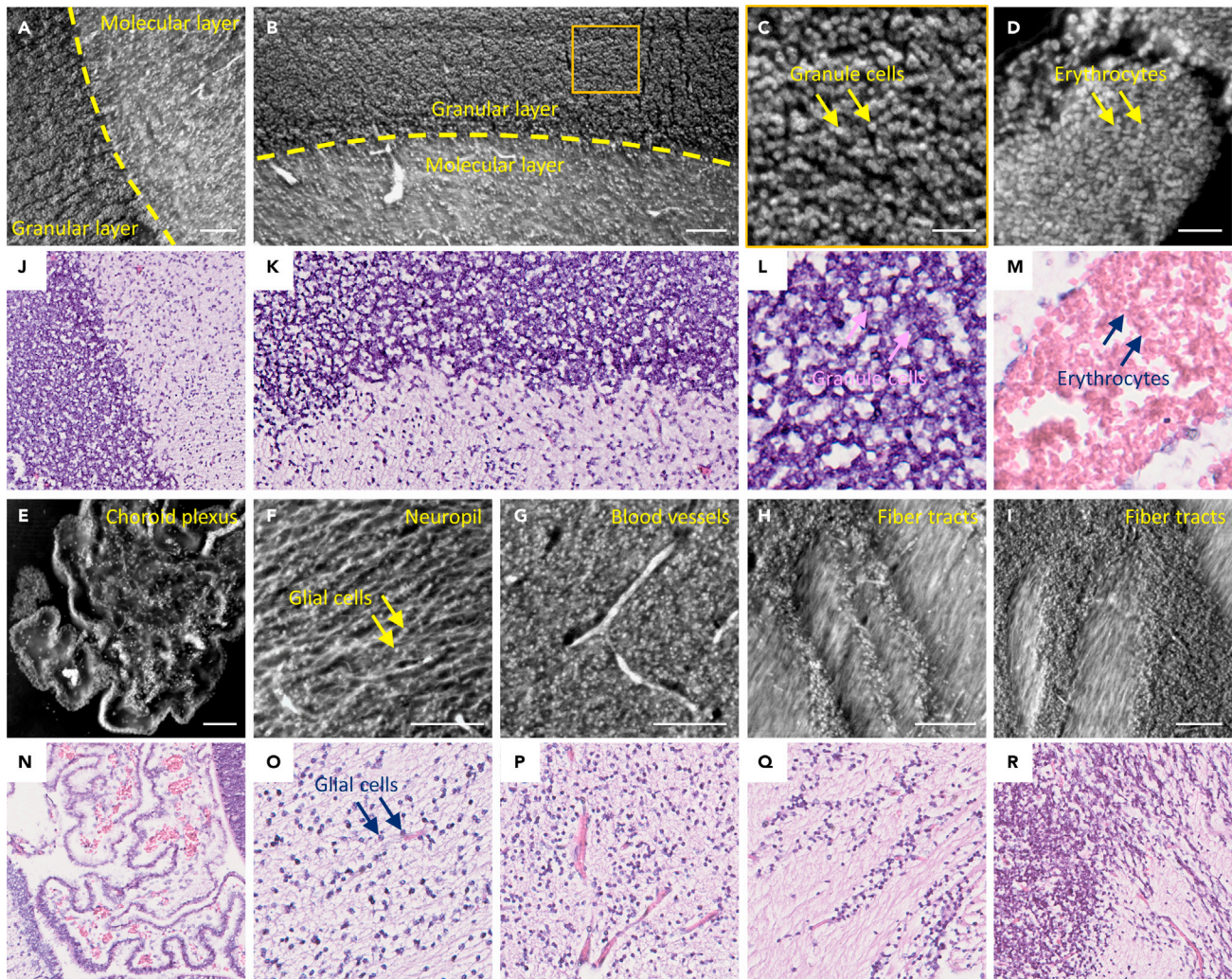


Figure 5. Image gallery of features extracted from label-free MATE images of the human brain block

(A and B) Cerebellar cortex, with the boundary between the granular layer and molecular layer marked by yellow dashed lines. Scale bars: 100 μ m.

(C) A zoomed-in MATE image of the orange solid region in B. Scale bar: 30 μ m.

(D) Erythrocytes. Scale bar: 30 μ m.

(E) Choroid plexus. Scale bar: 100 μ m.

(F) Neuropil. Scale bar: 100 μ m.

(G) Blood vessels. Scale bar: 100 μ m.

(H and I) Fiber tracts. Scale bars: 100 μ m.

(J–R) The corresponding features extracted from the H&E-stained histological images.

resolution (Figures 4I and 4J and Video S4). 3D projection of the region marked in Figure 4B is color coded in depth to characterize the vascular network of the human brain in space (Figure 4K).

Figure 5 shows a collection of histological features extracted from the human brain dataset (Figures 5A–5I). Several thin tissue slices were consecutively sectioned from the block surface and subsequently stained to obtain the closest H&E-stained histological images, which can serve as references of the imaged brain volume. The corresponding features extracted from these H&E-stained images are shown for comparison (Figures 5J–5R). Although these features cannot be identical to that in MATE images owing to the tissue perturbation during slide preparation, the cellular distributions are still remarkably similar. For instance, the boundary between the granular layer and molecular layer in the cerebellar cortex is clearly distinguished in both MATE and H&E-stained images (Figures 5A, 5B, 5J, and 5K). The densely packed granule cells and erythrocytes are resolved with high correspondence (Figures 5C, 5D, 5L, and 5M). Other

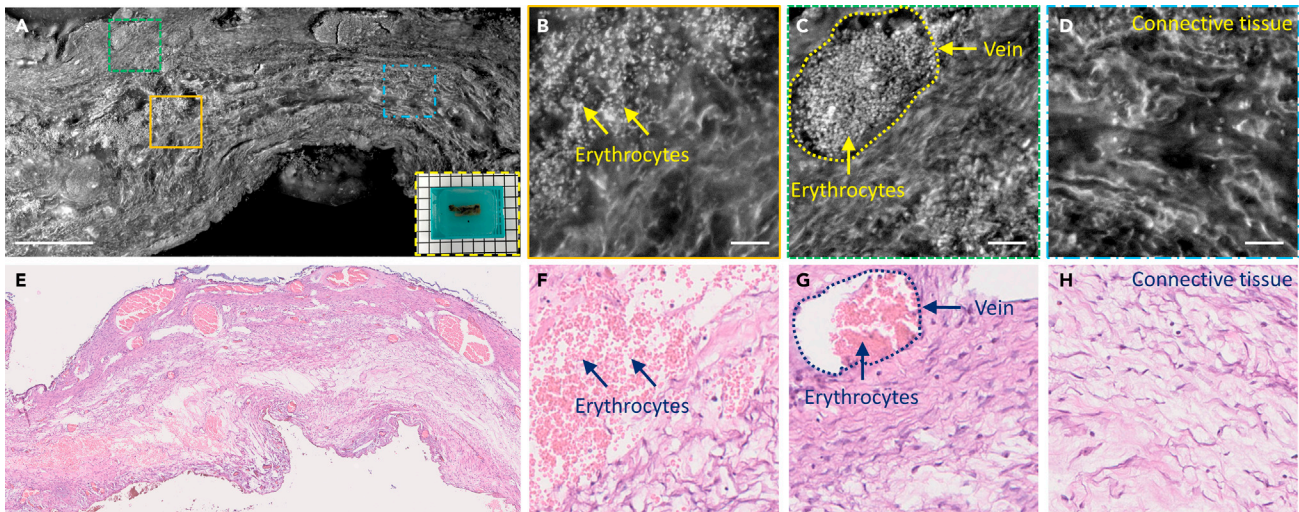


Figure 6. MATE imaging of an FFPE human gallbladder block

(A) A MATE image of an FFPE human gallbladder block, inset at the bottom right shows the photograph of the specimen. Scale bar: 500 μ m. (B–D) Zoomed-in MATE images of orange solid, green dashed, and blue dashed regions in A, respectively. Scale bars: 50 μ m. (E–H) The corresponding H&E-stained histological images.

anatomical structures, including choroid plexus (Figure 5E), neuropil (Figure 5F), blood vessels (Figure 5G), and myelinated fibers (Figures 5H and 5I) are simultaneously visualized by MATE in a label-free setting that otherwise would require tissue clearing and multiple fluorescent probes for revealing them as mentioned in the previously reported method (Morawski et al., 2018). MATE enables label-free histological imaging of complex tissue networks by non-specific excitation of various biomolecules with minimal tissue preparation, demonstrating its unique superiority as a routine 3D imaging platform. MATE can potentially fit into the current clinical practice to facilitate comprehensive histopathological interpretation at the cellular level, hence understanding organs in 3D instead of 2D slices.

MATE imaging of an FFPE human gallbladder block

Finally, an FFPE human gallbladder block is imaged by MATE (Figures 6A–6D). Similarly, the block is consecutively sectioned and stained to obtain the corresponding H&E-stained images for comparison (Figures 6E–6H). Although tissue deformation occurs during microtome sectioning and slide mounting, molecular features such as erythrocytes (Figures 6B and 6F) in the veins (Figures 6C and 6G) and anatomical features such as perimuscular connective tissue (Figures 6D and 6H) are well characterized in both MATE and H&E-stained images with high fidelity, validating the feasibility of using MATE to image different organs.

DISCUSSION

MATE is a promising and transformative 3D histological imaging platform that enables rapid and comprehensive histopathological analysis of complex whole organs without tissue staining or clearing. However, there are still deviations between MATE and H&E-stained histological images. First, the nucleoli structures are better observed in H&E-stained images than in MATE under the same magnification (e.g., Figures S4I, S4L, S5B, and S5H). This is likely because the fluorescence property of nucleoli in the detected spectral range is not chemically identical to that in the histological stains. Second, the texture of fiber tracts in the white matter of the human brain is better visualized in MATE than in H&E-stained images (e.g., Figures 5H, 5I, 5Q, and 5R). This is possibly due to the proteins in these fibrous structures presenting a high quantum yield under deep-UV excitation while eosin exhibits similar affinity across the cytoplasm.

Intrinsic fluorescence excited by deep-UV light naturally forms a contrast mechanism for high-content label-free imaging, but it varies significantly among different types of tissues/biomolecules and tissue processing. For instance, tissue fixation can significantly affect imaging performance (Figure S9). In general, the autofluorescence intensity tends to increase with the fixation duration, leading to a degraded negative contrast of cell nuclei in MATE images. In addition, cells will burst with a high concentration of formalin,

which is detrimental to probe cellular features. In addition, the fluorescence from erythrocytes, generated by photodecomposition of hemoglobin with deep-UV irradiation, is sensitive to reactive oxygen species (Pan et al., 2012), thus presenting different fluorescence intensity among thin tissue slices (denoted by asterisks in Figure S4). Furthermore, MATE allows simultaneous visualization of cell nuclei, fiber tracts, and blood vessels by non-specific excitation of various biomolecules, posing a challenge to accurate segmentation of clinically relevant image features. We believe that this problem can be solved by using advanced neural networks, which would enable a more faithful tissue analysis (Al-Kofahi et al., 2018).

MATE is currently in an early stage of development. The technical improvements can be further realized in terms of imaging speed and spatial resolution. MATE enables 3D reconstruction of 1 cm^3 tissue volume at $1.2 \times 1.2 \times 10\ \mu\text{m}^3$ voxel resolution within 4 h in the current setting. The imaging speed is mainly limited by the relatively weak autofluorescence intensity and repeated mechanical sectioning process. The acquisition speed can be further accelerated by (1) employing multiple high-power UV-LEDs to minimize the camera integration time for each image tile, (2) using a camera with a large chip size to reduce the total in-plane acquisitions, (3) using high-speed motorized stages for fast mechanical sectioning, and (4) applying contour detection to avoid unnecessary background acquisitions. To maintain a high image signal-to-noise ratio, the exposure time for each image tile was set to 100 ms with a single UV-LED illumination, resulting in an in-plane acquisition speed of $\sim 6\text{ s/cm}^2$. To provide sufficient space for handling the sliced tissues, the distance between the objective lens and blade was fixed to 5 cm, and the translational stage was moved at a velocity of 15 mm/s to minimize the sectioning artifacts introduced by our laboratory-built microtome (e.g., blade vibration and paraffin debris), such that it takes $\sim 7\text{ s}$ for each sectioning process. We expect that the imaging speed can be accelerated by two times in the future design by implementing multiple high-power illumination sources, commercial microtome, and high-speed motorized stages. Note that MATE is a diffraction-limited imaging system in which the lateral resolution is restricted by the objective's numerical aperture (NA). We employed a $10\times/0.3\text{-NA}$ objective lens with a depth of field (DOF) of $\sim 8\ \mu\text{m}$ in this work, which is sufficient to visualize different anatomical structures at subcellular resolution. In addition, this objective lens can achieve the optimal imaging quality because the DOF matches the optical sectioning thickness provided by the UV surface excitation. The lateral resolution can be further improved by our recently proposed method with computational microscopy (Zhang et al., 2021a) at the expense of the increased computational burden. For axial direction, UV absorption from the embedded tissues is the current limiting factor for axial resolution, which is measured to be $\sim 10\ \mu\text{m}$ in our experiments. By integrating with structured illumination microscopy (Gong et al., 2016), or doping the sample embedding media with strong UV-absorbing dyes (Guo et al., 2019), the axial resolution is expected to be enhanced by an order of magnitude, facilitating diverse applications that require high voxel resolution such as long-range axon tracking and capillary network mapping in whole-brain imaging. Furthermore, virtually stained MATE images can be generated with the assistance of unsupervised learning (Tschuchnig et al., 2020; Zhang et al., 2021a), eliminating any training for pathologists in image interpretation for diagnostic decision-making.

In summary, we developed a label-free, automated, and ready-to-use 3D imaging technique that can be used routinely for comprehensive 3D histopathological analysis of complex and bulky tissues. With the combination of block-face imaging and serial microtome sectioning, MATE enables rapid and label-free imaging of paraffin-embedded whole organs at an acquisition speed of 1 cm^3 per 4 h with a voxel resolution of $1.2 \times 1.2 \times 10\ \mu\text{m}^3$. We showed that different anatomical structures, including cell nuclei, fiber tracts, and blood vessels in mouse/human brains, can be simultaneously visualized in MATE without tissue staining or clearing. In addition, diagnostic features, such as nuclear size and packing density, can be quantitatively extracted from MATE with high accuracy. As an augment to the current slide-based 2D histology, MATE holds great promise for studying a variety of disease processes in 3D, which should be carried out as follow-up work.

Limitations of the study

Although exogenous labels are not required for MATE imaging, significant variations in autofluorescence intensity can still be observed in MATE images as the excitation light is scattered/absorbed differently among various tissue types and functional areas (e.g., white matter and gray matter of the brain). In addition, tissue processing with chemical reagents during fixation and embedding may further exacerbate this variability. Furthermore, with continuous UV exposure, the overall intensity is progressively increased and the resulting homogeneously distributed autofluorescence adversely degrades the negative contrast of MATE.

STAR★METHODS

Detailed methods are provided in the online version of this paper and include the following:

- **KEY RESOURCES TABLE**
- **RESOURCE AVAILABILITY**
 - Lead contact
 - Materials availability
 - Data and code availability
- **METHOD DETAILS**
 - Collection of biological tissues
 - Configuration of the MATE system
 - Image analysis

SUPPLEMENTAL INFORMATION

Supplemental information can be found online at <https://doi.org/10.1016/j.isci.2021.103721>.

ACKNOWLEDGMENTS

The Translational and Advanced Bioimaging Laboratory (TAB-Lab) at HKUST acknowledges the pathology department from the Prince of Wales Hospital for providing the human samples. We also acknowledge the support of the Hong Kong Innovation and Technology Commission (ITS/036/19) and the Research Grants Council of the Hong Kong Special Administrative Region (26203619 and 16208620).

AUTHOR CONTRIBUTIONS

Y.Z., L.K., and T.T.W.W. conceived the study. Y.Z. and L.K. built the imaging system. Y.Z., L.K., and V.T.C.T. prepared the specimens involved in this study. Y.Z. performed imaging experiments. L.K. performed histological staining. Y.Z. processed and analyzed the data. Y.Z. and T.T.W.W. wrote the manuscript. T.T.W.W. supervised the whole study.

DECLARATION OF INTERESTS

V.T.C.T. and T.T.W.W. have financial interest in PhoMedics Limited, which, however, did not support this work. All authors declare no competing financial interests.

Received: September 30, 2021

Revised: November 24, 2021

Accepted: December 28, 2021

Published: January 21, 2022

REFERENCES

- Al-Kofahi, Y., Zaltsman, A., Graves, R., Marshall, W., and Rusu, M. (2018). A deep learning-based algorithm for 2-D cell segmentation in microscopy images. *BMC Bioinformatics* 19, 365. <https://doi.org/10.1186/s12859-018-2375-z>.
- Boonstra, H., Oosterhuis, J.W., Oosterhuis, A.M., and Fleuren, G.J. (1983). Cervical tissue shrinkage by formaldehyde fixation, paraffin wax embedding, section cutting and mounting. *Virchows Arch. A. Pathol. Anat. Histopathol* 402, 195–201. <https://doi.org/10.1007/BF00695061>.
- Busse, M., Müller, M., Kimm, M.A., Ferstl, S., Allner, S., Achterhold, K., Herzen, J., and Pfeiffer, F. (2018). Three-dimensional virtual histology enabled through cytoplasm-specific X-ray stain for microscopic and nanoscopic computed tomography. *Proc. Natl. Acad. Sci. U S A* 115, 2293–2298. <https://doi.org/10.1073/PNAS.1720862115/-/DCSUPPLEMENTAL>.
- Conchello, J.A., and Lichtman, J.W. (2005). Optical sectioning microscopy. *Nat. Methods*, 920–931. <https://doi.org/10.1038/nmeth815>.
- Davis, H.C., Ramesh, P., Bhatnagar, A., Lee-Gosselin, A., Barry, J.F., Glenn, D.R., Walsworth, R.L., and Shapiro, M.G. (2018). Mapping the microscale origins of magnetic resonance image contrast with subcellular diamond magnetometry. *Nat. Commun.* 9, 1–9. <https://doi.org/10.1038/s41467-017-02471-7>.
- Denk, W., and Horstmann, H. (2004). Serial block-face scanning electron microscopy to reconstruct three-dimensional tissue nanostructure. *PLoS Biol.* 2, e329. <https://doi.org/10.1371/JOURNAL.PBIO.0020329>.
- Dotd, H.U., Leischner, U., Schierloh, A., Jährling, N., Mauch, C.P., Deininger, K., Deussing, J.M., Eder, M., Zieglgänsberger, W., and Becker, K. (2007). Ultramicroscopy: three-dimensional visualization of neuronal networks in the whole mouse brain. *Nat. Methods* 4, 331–336. <https://doi.org/10.1038/nmeth1036>.
- Economou, M.N., Clack, N.G., Lavis, L.D., Gerfen, C.R., Svoboda, K., Myers, E.W., and Chandrashekar, J. (2016). A platform for brain-wide imaging and reconstruction of individual neurons. *eLife* 5, 1–22. <https://doi.org/10.7554/eLife.10566>.
- Fereidouni, F., Harmany, Z.T., Tian, M., Todd, A., Kintner, J.A., McPherson, J.D., Borowsky, A.D., Bishop, J., Lechpammer, M., Demos, S.G., and Levenson, R. (2017). Microscopy with ultraviolet surface excitation for rapid slide-free histology. *Nat. Biomed. Eng.* 1, 957–966. <https://doi.org/10.1038/s41551-017-0165-y>.
- Gong, H., Zeng, S., Yan, C., Lv, X., Yang, Z., Xu, T., Feng, Z., Ding, W., Qi, X., Li, A., et al. (2013). Continuously tracing brain-wide long-distance axonal projections in mice at a one-micron voxel

- resolution. *NeuroImage* 74, 87–98. <https://doi.org/10.1016/j.neuroimage.2013.02.005>.
- Gong, H., Xu, D., Yuan, J., Li, X., Guo, C., Peng, J., Li, Y., Schwarz, L.A., Li, A., Hu, B., et al. (2016). High-throughput dual-colour precision imaging for brain-wide connectome with cytoarchitectonic landmarks at the cellular level. *Nat. Commun.* 7, 12142. <https://doi.org/10.1038/ncomms12142>.
- Guo, J., Artur, C., Eriksen, J.L., and Mayerich, D. (2019). Three-dimensional microscopy by milling with ultraviolet excitation. *Sci. Rep.* 9, 14578–14579. <https://doi.org/10.1038/s41598-019-50870-1>.
- Helmchen, F., and Denk, W. (2005). Deep tissue two-photon microscopy. *Nat. Methods* 2, 932–940. <https://doi.org/10.1038/nmeth818>.
- Huisken, J., Swoger, J., Del Bene, F., Wittbrodt, J., and Stelzer, E.H. (2004). Optical sectioning deep inside live embryos by selective plane illumination microscopy. *Science* 305, 1007–1009. <https://doi.org/10.1126/science.1100035>.
- Jamme, F., Kascakova, S., Villette, S., Allouche, F., Pallu, S., Rouam, V., and Réfrégiers, M. (2013). Deep UV autofluorescence microscopy for cell biology and tissue histology. *Biol. Cell* 105, 277–288. <https://doi.org/10.1111/boc.201200075>.
- Jerman, T., Pernuš, F., Likar, B., and Spiclin, Z. (2015). Beyond Frangi: an improved multiscale vesselness filter. In *Medical Imaging 2015: Image Processing*, S. Ourselin and M.A. Styner, eds. (SPIE), p. 94132A. <https://doi.org/10.1117/12.2081147>.
- Juliana, J.M., Zanette, I., Noël, P.B., Cardoso, M.B., Kimm, M.A., and Pfeiffer, F. (2015). Three-dimensional non-destructive soft-tissue visualization with X-ray staining micro-tomography. *Scientific Rep.* 5, 1–7. <https://doi.org/10.1038/srep14088>.
- Katsamenis, O.L., Olding, M., Warner, J.A., Chatelet, D.S., Jones, M.G., Sgalla, G., Smit, B., Larkin, O.J., Haig, I., Richeldi, L., et al. (2019). X-ray micro-computed tomography for nondestructive three-dimensional (3D) X-ray histology. *Am. J. Pathol.* 189, 1608–1620. <https://doi.org/10.1016/j.ajpath.2019.05.004>.
- Li, A., Gong, H., Zhang, B., Wang, Q., Yan, C., Wu, J., Liu, Q., Zeng, S., and Luo, Q. (2010). Micro-optical sectioning tomography to obtain a high-resolution atlas of the mouse brain. *Science* 330, 1404–1408. <https://doi.org/10.1126/science.1191776>.
- Li, L., Xia, J., Li, G., Garcia-Urbe, A., Sheng, Q., Anastasio, M.A., and Wang, L.V. (2016). Label-free photoacoustic tomography of whole mouse brain structures ex vivo. *Neurophotonics* 3, 035001. <https://doi.org/10.1117/1.NPH.3.3.035001.4>.
- Marx, V. (2016). Optimizing probes to image cleared tissue. *Nat. Methods* 13, 205–209. <https://doi.org/10.1038/nmeth.3774>.
- Meinhardt, M., Krebs, R., Anders, A., Heinrich, U., and Tronnier, H. (2008). Wavelength-dependent penetration depths of ultraviolet radiation in human skin. *J. Biomed. Opt.* 13, 044030. <https://doi.org/10.1117/1.2957970>.
- Mertz, J. (2011). Optical sectioning microscopy with planar or structured illumination. *Nat. Methods* 8, 811–819. <https://doi.org/10.1038/nmeth.1709>.
- Min, E., Ban, S., Lee, J., Vavilin, A., Baek, S., Jung, S., Ahn, Y., Park, K., Shin, S., Han, S., et al. (2020). Serial optical coherence microscopy for label-free volumetric histopathology. *Sci. Rep.* 10, 6711–6718. <https://doi.org/10.1038/s41598-020-63460-3>.
- Moehrl, M., Dietz, K., Garbe, C., and Breuninger, H. (2006). Conventional histology vs. three-dimensional histology in lentigo maligna melanoma. *Br J Dermatol.* 154, 453–459. <https://doi.org/10.1111/j.1365-2133.2005.07068.x>.
- Monici, M. (2005). Cell and tissue autofluorescence research and diagnostic applications. *Biotechnol. Annu. Rev.* 227–256. [https://doi.org/10.1016/S1387-2656\(05\)11007-2](https://doi.org/10.1016/S1387-2656(05)11007-2).
- Morawski, M., Kirilina, E., Scherf, N., Jäger, C., Reimann, K., Trampel, R., Gavrilidis, F., Geyer, S., Biedermann, B., Arendt, T., and Weiskopf, N. (2018). Developing 3D microscopy with CLARITY on human brain tissue: towards a tool for informing and validating MRI-based histology. *NeuroImage* 182, 417–428. <https://doi.org/10.1016/j.neuroimage.2017.11.060>.
- Narasimhan, A., Venkataraju, K.U., Mizrahi, J., Albeanu, D.F., and Osten, P. (2015). Oblique light-sheet tomography: fast and high resolution volumetric imaging of mouse brains. *bioRxiv* 132423. <https://doi.org/10.1101/132423>.
- Pan, L., Wang, X., Yang, S., Wu, X., Lee, I., Zhang, X., Rupp, R.A., and Xu, J. (2012). Ultraviolet irradiation-dependent fluorescence enhancement of hemoglobin catalyzed by reactive oxygen species. *PLoS One* 7, e441142. <https://doi.org/10.1371/journal.pone.0044142>.
- Peng, T., Thorn, K., Schroeder, T., Wang, L., Theis, F.J., Marr, C., and Navab, N. (2017). A BaSiC tool for background and shading correction of optical microscopy images. *Nat. Commun.* 8, 14836–14837. <https://doi.org/10.1038/ncomms14836>.
- Pichat, J., Iglesias, J.E., Yousry, T., Ourselin, S., and Modat, M. (2018). A survey of methods for 3D histology reconstruction. *Med. Image Anal.* 46, 73–105. <https://doi.org/10.1016/j.media.2018.02.004>.
- Ragan, T., Kadiri, L.R., Venkataraju, K.U., Bahlmann, K., Sutin, J., Taranda, J., Arganda-Carreras, I., Kim, Y., Seung, H.S., and Osten, P. (2012). Serial two-photon tomography for automated ex vivo mouse brain imaging. *Nat. Methods* 9, 255–258. <https://doi.org/10.1038/nmeth.1854>.
- Renier, N., Wu, Z., Simon, D.J., Yang, J., Ariel, P., and Tessier-Lavigne, M. (2014). IDISCO: a simple, rapid method to immunolabel large tissue samples for volume imaging. *Cell* 159, 896–910. <https://doi.org/10.1016/j.cell.2014.10.010>.
- Richardson, D.S., and Lichtman, J.W. (2015). Clarifying tissue clearing. *Cell*, 246–257. <https://doi.org/10.1016/j.cell.2015.06.067>.
- Roberts, N., Magee, D., Song, Y., Brabazon, K., Shires, M., Crellin, D., Orsi, N.M., Quirke, R., Quirke, P., and Treanor, D. (2012). Toward routine use of 3D histopathology as a research tool. *Am. J. Pathol.* 180, 1835–1842. <https://doi.org/10.1016/j.ajpath.2012.01.033>.
- Salvolini, L., Bichi Secchi, E., Costarelli, L., and De Nicola, M. (2000). Clinical applications of 2D and 3D CT imaging of the airways—a review. *Eur. J. Radiol.* 34, 9–25. [https://doi.org/10.1016/S0720-048X\(00\)00155-8](https://doi.org/10.1016/S0720-048X(00)00155-8).
- Schindelin, J., Arganda-Carreras, I., Frise, E., Kaynig, V., Longair, M., Pietzsch, T., Preibisch, S., Rueden, C., Saalfeld, S., Schmid, B., et al. (2012). Fiji: an open-source platform for biological-image analysis. *Nat. Methods* 9, 676–682. <https://doi.org/10.1038/nmeth.2019>.
- Seiriki, K., Kasai, A., Hashimoto, T., Schulze, W., Niu, M., Yamaguchi, S., Nakazawa, T., Inoue, K.I., Uezono, S., Takada, M., et al. (2017). High-speed and scalable whole-brain imaging in rodents and primates. *Neuron* 94, 1085–e6. <https://doi.org/10.1016/j.neuron.2017.05.017>.
- Tomer, R., Ye, L., Hsueh, B., and Deisseroth, K. (2014). Advanced clarity for rapid and high-resolution imaging of intact tissues. *Nat. Protoc.* 9, 1682–1697. <https://doi.org/10.1038/nprot.2014.123>.
- Tran, T., Sundaram, C.P., Bahler, C.D., Eble, J.N., Grignon, D.J., Monn, M.F., Simper, N.B., and Cheng, L. (2015). Correcting the shrinkage effects of formalin fixation and tissue processing for renal tumors: toward standardization of pathological reporting of tumor size. *J. Cancer* 6, 759–766. <https://doi.org/10.7150/jca.12094>.
- Tschuchnig, M.E., Oostingh, G.J., and Gademayr, M. (2020). Generative adversarial networks in digital pathology: a survey on trends and future potential. *Patterns (N Y)* 1, 100089. <https://doi.org/10.1016/j.patter.2020.100089>.
- Wang, C.W., Budiman Gosno, E., and Li, Y.S. (2015). Fully automatic and robust 3D registration of serial-section microscopic images. *Sci. Rep.* 5, 15051–15114. <https://doi.org/10.1038/srep15051>.
- Wong, T.T.W., Zhang, R., Zhang, C., Hsu, H.C., Maslov, K.I., Wang, L., Shi, J., Chen, R., Shung, K.K., Zhou, Q., and Wang, L.V. (2017). Label-free automated three-dimensional imaging of whole organs by microtomy-assisted photoacoustic microscopy. *Nat. Commun.* 8, 1386. <https://doi.org/10.1038/s41467-017-01649-3>.
- Xiao, G., Bloch, B.N., Chappelow, J., Genega, E.M., Rofsky, N.M., Lenkinski, R.E., Tomaszewski, J., Feldman, M.D., Rosen, M., and Madabhushi, A. (2011). Determining histology-MRI slice correspondences for defining MRI-based disease signatures of prostate cancer. *Comput. Med. Imaging Graph* 35, 568–578. <https://doi.org/10.1016/J.COMMEDIMAG.2010.12.003>.
- Yao, J., and Wang, L.V. (2013). Photoacoustic microscopy. *Laser Photon. Rev.* 7, 758–778. <https://doi.org/10.1002/LPOR.201200060>.
- Yoshitake, T., Giacomelli, M.G., Quintana, L.M., Vardeh, H., Cahill, L.C., Faulkner-Jones, B.E., Connolly, J.L., Do, D., and Fujimoto, J.G. (2018). Rapid histopathological imaging of skin and breast cancer surgical specimens using immersion microscopy with ultraviolet surface excitation. *Sci. Rep.* 8, 4476–4512. <https://doi.org/10.1038/s41598-018-22264-2>.

Zhang, Y., Kang, L., Wong, I.H.M., Dai, W., Li, X., Chan, R.C.K., Hsin, M.K.Y., and Wong, T.T.W. (2021a). High-throughput, label-free and slide-free histological imaging by computational microscopy and unsupervised learning. *Adv. Sci.* 2102358. <https://doi.org/10.1002/ADVS.202102358>.

Zhang, Y., Kang, L., Yu, W., Tsang, V.T.C., and Wong, T.T.W. (2021b). Three-dimensional label-free histological imaging of whole organs by microtomy-assisted autofluorescence tomography. Mendeley Data. <https://doi.org/10.17632/nkxw97h6c.2>.

Zheng, T., Feng, Z., Wang, X., Jiang, T., Jin, R., Zhao, P., Luo, T., Gong, H., Luo, Q., and Yuan, J. (2019). Review of micro-optical sectioning tomography (MOST): technology and applications for whole-brain optical imaging [Invited]. *Biomed. Opt. Express* 10, 4075–4096. <https://doi.org/10.1364/boe.10.004075>.

STAR★METHODS

KEY RESOURCES TABLE

REAGENT or RESOURCE	SOURCE	IDENTIFIER
Biological samples		
Fixed mouse brain	This paper	N/A
Fixed human brain	Prince of Wales Hospital	N/A
Fixed human gallbladder	Prince of Wales Hospital	N/A
Deposited data		
Raw and processed data	This paper	(Zhang et al., 2021b). Mendeley Data: https://doi.org/10.17632/nkvxw97h6c.2
LabVIEW code for system mechanical control	This paper	(Zhang et al., 2021b). Mendeley Data: https://doi.org/10.17632/nkvxw97h6c.2
MATLAB code for batch image stitching	This paper	(Zhang et al., 2021b). Mendeley Data: https://doi.org/10.17632/nkvxw97h6c.2
Software and algorithms		
Avizo	Thermo Fisher Scientific	https://www.thermofisher.com/hk/en/home/electron-microscopy/products/software-em-3d-vis/avizo-software.html
Fiji	(Schindelin et al., 2012)	https://imagej.net/software/fiji/
Flat-field correction	(Peng et al., 2017)	http://sites.imagej.net/BaSiC/
Jerman's spherical enhancement filter	(Jerman et al., 2015)	https://github.com/timjerman/JermanEnhancementFilter
Other		
UV-LED	Thorlabs	M285L5
Single-band bandpass filter	Semrock	FF01-285/14-25
Aspheric lens	Edmund Optics	#33-957
Plano-convex lens	Thorlabs	LA4148-UV
Plan achromat objective lens	Olympus	UPLFLN10X2
Infinity-corrected tube lens	Thorlabs	TTL180-A
Monochrome camera	PCO	pco.edge 4.2
3-axis motorized stage	PI miCos GmbH	L-509.20SD00
Fluorescent beads	Thermo Fisher Scientific	B200
Microtome	Leica Microsystems	RM2235
Whole-slide scanner	Hamamatsu Photonics	NanoZoomer-SQ

RESOURCE AVAILABILITY

Lead contact

Further information and requests for reagents and resources should be directed to and will be fulfilled by the lead contact, Terence T. W. Wong (ttwong@ust.hk).

Materials availability

This study did not generate new unique reagents.

Data and code availability

- DATA have been deposited at Mendeley Data and are publicly available as of the date of publication. DOIs are listed in the [key resources table](#).

- All original code has been deposited at Mendeley Data and is publicly available as of the date of publication. DOIs are listed in the [key resources table](#).
- Any additional information required to reanalyze the data reported in this paper is available from the lead contact upon request.

METHOD DETAILS

Collection of biological tissues

C57BL/6 mice were euthanized by CO₂. The brain tissue was then harvested from the mice immediately and fixed in 4% neutral-buffered formalin at room temperature for 24 hours, followed by standard FFPE tissue preparation protocol and paraffin-embedded as block specimens for MATE imaging. To prepare thin tissue slices for validation, the block specimens were sectioned at the surface by a microtome (RM2235, Leica Microsystems Inc.) with 7- μ m thickness and stained by H&E, and subsequently imaged by a digital slide scanner (NanoZoomer-SQ, Hamamatsu Photonics K.K.) to generate the corresponding histological images. All experiments were carried out in conformity with a laboratory animal protocol approved by the Health, Safety and Environment Office of Hong Kong University of Science and Technology (HKUST). The human sample protocol was approved by the Institutional Review Board at the Prince of Wales Hospital. The imaged tissue was considered as leftover tissue, i.e., it represents a portion of a collected specimen that is not needed for assessment of diagnostic, prognostic, and other parameters in the diagnosis and treatment of the patient.

Configuration of the MATE system

As shown in [Figure 1](#), the MATE system is configured in a reflection mode to accommodate tissues with any size and thickness. A UV-LED (285-nm wavelength, M285L5, Thorlabs Inc.) is spectrally filtered by a band-pass filter (FF01-285/14-25, Semrock Inc.) and obliquely focused onto the bottom surface of the specimen through a pair of relay lenses (#33-957, Edmund Optics Inc., and LA4148-UV, Thorlabs Inc.). The excitation power is measured to be 100 mW with an illumination area of ~ 1 mm². Oblique illumination circumvents the use of any UV-transmitting optics and fluorescence filters because the backscattered UV light is naturally blocked by the glass objective and tube lens which are spectrally opaque at 285 nm. The UV-excited intrinsic fluorescence is detected by an inverted microscope which consists of a plan achromat objective lens (Plan Fluor, 10 \times /0.3 NA, Olympus Corp.) and an infinity-corrected tube lens (TTL180-A, Thorlabs Inc.), and subsequently imaged by a monochrome scientific complementary metal-oxide-semiconductor camera (PCO edge 4.2, 2048 \times 2048 pixels, 6.5- μ m pixel pitch, PCO. Inc.) which can theoretically reach an imaging throughput of ~ 800 megabytes/s. The paraffin-embedded specimen is clamped towards the objective lens by an adjustable sample holder, and rigidly mounted on a 3-axis motorized stage (L-509.20SD00, 1- μ m bidirectional repeatability, PI miCos GmbH) to control both x-y scanning at 1.2-mm interval for in-plane mosaic imaging, and z scanning at the 10- μ m interval for microtome sectioning. The lab-built microtome is tuned with a cutting angle of $\sim 30^\circ$, and placed conjugated with the objective's focal plane to obtain sharp in-focus images. The thin tissue slices are sliced off and dropped down due to the gravity and collected in a collection area. To balance acquisition speed, image quality, and sectioning stability, the motorized stage is translated at a velocity of 15 mm/s for microtome sectioning, and the acquisition time for each in-plane image tile is set to 110 ms (100-ms camera integration time plus 10-ms stage settling time). The captured image tiles are stitched during image acquisition, which is synchronized with motor scanning via our lab-designed LabVIEW software (National Instruments Corp.) and triggering circuits. The system is fully automated to provide a series of distortion- and registration-free images with intrinsic absorption-based contrast, enabling rapid and label-free 3D imaging of paraffin-embedded whole organs at an acquisition speed of 1 cm³ per 4 hours. The lateral resolution of MATE was characterized by imaging 200-nm-diameter fluorescent beads (B200, emission at 445 nm, Thermo Fisher Scientific Inc.), and the full width at half maximum is measured to be 1.2 μ m ([Figure S3](#)).

Image analysis

The captured raw image tiles were first processed with flat-field correction ([Peng et al., 2017](#)) to minimize illuminance non-uniformity, and then stitched by a customized linear blending method. Flat-field correction is an important step before in-plane image stitching, which can effectively mitigate the shading artifact and ensure a seamless mosaic image ([Figure S10](#)). Stack registration of different axial layers is not necessary due to the high bidirectional repeatability (± 1 μ m) of the employed translational stages.

MATE and H&E-stained histological images were segmented by a free Fiji plugin (trainable Weka segmentation), and subsequently binarized and analyzed in Fiji to acquire the cross-sectional area and centroid of each cell nucleus. With the localized center positions of cell nuclei, the intercellular distance was calculated to be the shortest adjacent distance to a neighboring cell nucleus. To generate a nuclear density map, the MATE images were processed by a Jerman's spherical enhancement filter ([Jerman et al., 2015](#)), and subsequently binarized and analyzed in Fiji to localize each cell nucleus. After that, the center positions of the cell nuclei in the image were set to unit-amplitude against a zero-amplitude background, in which cell counting was performed in every $50\ \mu\text{m} \times 50\ \mu\text{m}$ surrounding area and normalized to generate the nuclear density map (detailed method shown in [Figure S7](#)). The serial registration-free block-face images were processed and rendered in Avizo software (Thermo Fisher Scientific Inc.) for 3D visualization.